Desalination and Water Treatment
www.deswater.com
doi: 10.5004/dwt.2019.24338

162 (2019) 97–111
September

Graphene-based aerogels with carbon nanotubes as ultrahigh-performing mesoporous capacitive deionization electrodes for brackish and seawater desalination

Sanju Gupta*, Alex Henson§, Brendan Evans§, Romney Meek

Department of Physics and Astronomy, Western Kentucky University, 1906 College Heights Blvd. Bowling Green, KY 42101, USA, emails: sanju.gupta@wku.edu (S. Gupta), alex.henson836@topper.wku.edu (A. Henson), brendan.evans054@topper.wku.edu (B. Evans), romney.meek@gmail.com (R. Meek)

Received 12 January 2019; Accepted 29 April 2019

ABSTRACT

As water scarcity has become a serious global issue, capacitive deionization (CDI) with high energy efficiency and cost effectiveness is considered a promising desalination technique to address this problem and produce potable freshwater. In this work, we rationally designed nanomaterials with three-dimensional porous architectures that have been an urgent need for CDI application. We strategically prepared graphene-based novel 'hybrid' aerogels interspersed with multi-walled carbon nanotubes (Gr-MWCNT) and their nitrogenated analogs (N-Gr-MWCNT) as mesoporous CDI electrodes using a facile hydrothermal synthesis method. The three-dimensional monolith aerogels show (a) topologically interconnected network of graphene nanosheets (GNS) with, (b) hierarchical in-plane porosity with uniform strut size having, (c) higher specific surface area, (d) good electrical conductivity, and (e) wettability, resulting in efficient salt ion electrosorption capacity and pathways for ion transportation which allowed achieving ultrahigh desalination performance during CDI process. We also studied CDI electrodes made from holey graphene (hG) of narrow pore size and precursor graphene oxide (GO_{film}) for comparison. As compared with other nanocarbons, three-dimensional graphene aerogels and hG feature a homogeneous nanoscale porosity, reasonable defects density and carbon edge sites besides moderate specific capacitance. The significant electrosorption capacity determined from isotherms ranged 20.1–22.5 mg g^{-1} at cell potential 1.8 V in 0.5 g L^{-1}. This could be attributed to the interconnected mesopores within the graphene sheet and carbon nanotube network that allows larger accessibility for ion adsorption. The results elucidate the interplay of mesoscale and nanoscale porosity, high chemical surface charge, oxygen and nitrogenated surface functional groups that are favorable for significantly improved CDI performance, by buffering ions to reduce the diffusion distance from saline water to the interior surfaces/interfaces of these 'hybrid' aerogels.

Keywords: Capacitive deionization; Holey graphene; Graphene aerogels; Electrosorption; Saline and seawater

1. Introduction

Water is life and scarcity of which is a crippling issue of global proportion. Based on a recent water development report from the United Nations, this problem will only worsen in the next two decades or so. Among technologies currently deployed to address water crisis, nanofiltration and desalination (via reverse osmosis, RO) besides thermal processes have emerged as key strategies to solve global water

* Corresponding author.

§ Student co-authors (A.H., B.E.) contributed equally to this work and student co-author (R.M.) helped in preparing aerogels.

paucity [1–5]. The use of RO filtration is increasingly used to produce clean water for growing world population, with greater than 50% of desalination plants worldwide using RO technology [6–8]. The RO process use semipermeable polymeric (e.g., polyamide; PA) and ceramic membranes under pressure applied greater than the osmotic pressure, producing potable freshwater by removing ions, molecules and larger particles [7]; it requires approximately 3 kW h of energy per kg to produce 1 m^3 of drinking water. However, these membranes suffer from limitation of high permeability (flux), salt ion rejection (retention), mechanical robustness, scalability, cost-effectiveness, and energy efficiency. Meanwhile, capacitive deionization (CDI) – an electrochemically controlled technique that follows the working principle of an electric double layer capacitor (EDLC) related to energy storage supercapacitors albeit with distinct variations – is gaining significant attention for desalination of both brackish and seawater [9–12]. It has demonstrated several key advantages including membrane-free technique, inexpensive, operates at low direct voltages thus can be energy efficient. However, recent paper by Qin et al. [12] compared the energy efficiency of RO and CDI techniques for desalination through modeling while taking into account of several useful parameters. They found that RO process consumes less energy by almost eight times than that of CDI method to produce 10 L m^{-2} h^{-1}. In spite of this, the CDI method is far more suitable for small-scale portable implementation, environmentally friendliness while lacking secondary pollution. When an external voltage is applied, undesired salt ionic species are electrosorbed on the double-layers formed between the solution (e.g., saline water) and the two oppositely charged porous electrode interface, known as charging-step (Fig. 1) [13]. Once the pores are saturated with ions, a reverse voltage or a short circuit is applied to regenerate the electrodes by desorbing ions (back in solution) is the discharging step and the next cycle begins. To achieve the desired desalination efficiency during multi cycles, CDI performance heavily relies upon physical–chemical properties and internal structure of electrode materials. In principle, the main factors that CDI electrodes should have are summarized as follows: high specific surface area and specific capacitance, good electrical conductivity or less resistance, robust chemical inertia, good wettability to water, faster charge/ion transportation, higher porosity, narrow pore size distribution, and high fouling resistance [4,14]. Therefore, increasing global demand for potable clean water due to population growth and accelerated industrialization calls for materials innovations not only for CDI but also for expansive field of nanoionics. The challenge remains to develop optimized nanostructured morphology, surface chemistry, pore size, pore interface density, and electrode thickness that are anticipated to play key roles in regulating salt adsorption capacity and rate while undergoing electrosorption process [5]. Moreover, ion conduction and ion adsorption are governed by interfacial effects and for a given material the density of interfaces matters, even locally and the importance of ionic charge carriers is by no means less than that of electronic charge carriers. These mesoscopic phenomena are at the heart of nanoionics [15].

Many carbon-based nanomaterials are investigated for CDI electrodes [16–18], as they meet most of the above-mentioned characteristics, include activated carbon (AC), carbon nanotubes (CNTs), activated graphene (AG), carbon nanofibers (CNF), carbon aerogels (CA), and ordered mesoporous carbon (OMC). The rise of graphene and graphene-related materials has fascinated scientists and engineers alike across several disciplines. Graphene-family nanomaterials (GFNs), in particular, are garnering widespread attention as potential game changer for sustainable water-related research pursuits. The well-known high hydrophobicity and low specific capacitance of AC and some other carbons are the main constraints preventing their wide usage in a pristine form and several attempts have been made to address these issues. GFNs include graphene oxide (GO), reduced graphene oxide (rGO), multilayer nanoporous graphene, graphene aerogels (GA), and heterogeneous atom doped graphene, further adds to the list attributed to their open and tunable structure and morphology, rich surface chemistry, tailored boundary interfaces and extraordinary physicochemical properties, particularly, high theoretical surface area (ca. 2,630 m^2 g^{-1}) as compared with CNTs which make them ideal candidate for CDI application. Due to the mass production and facile preparation, the most convenient ways is to synthesize GO followed by reduction (rGO) chemically or thermally. However, the reduction processes typically used causes GO and rGO sheets to agglomerate due to strong p–p interactions that lead to uncontrollable pore size distribution and low surface area, which significantly limit their practical usage in CDI performance. The most common method to overcome agglomeration is to add nanoscale 'spacers' between GO sheets. Various 'spacers' such as metal oxides, conductive polymers or carbon materials (e.g., CNTs) were chosen to be incorporated into the interlayers of graphene. Anchoring metal oxides (MnO_2, SnO_2, TiO_2, ZnO, and ZrO_2) nanoparticles onto nanocarbons increases the specific capacitance per area and charge efficiency as well as their hydrophilic properties, however, these 'hybrid' composites do not yet perform as well as desired for CDI [4]. Constructing three-dimensional (3D) graphene with macroporous structure is another effective approach to prohibit restacking [19,20]. Recently, graphene nanosheets (GNS) containing high density of nanopores in their basal planes have been explored and while there are studies showing their applications toward energy storage and conversion devices, molecular gas separation, the potential role in water desalination remains largely less explored [21,22]. Henceforth, rationally designed mesoporous carbon monoliths of higher specific surface area with hierarchical pore size distribution as electrode materials and electrical conductivity are the prime factors for efficient electrosorption of salt and other charged species. Herein, we propose novel CDI electrodes based on three-dimensional architectures composed of graphene-multiwalled carbon nanotubes (Gr-MWCNT) aerogels and their nitrogenated analogs (N-Gr-MWCNTs) synthesized using scalable and facile hydrothermal synthetic approach followed by freeze-drying to transform hydrogels into aerogels. They are composed of multiplexed morphology and hierarchical in-plane mesoscale and nanoscale porosity with several interconnected lamellar nodes. The as-prepared Gr-MWCNT aerogels showed high surface area of 570 m^2 g^{-1} and specific capacitance besides fast ion adsorption. To the best of our knowledge, there have not been reports on the fabrication

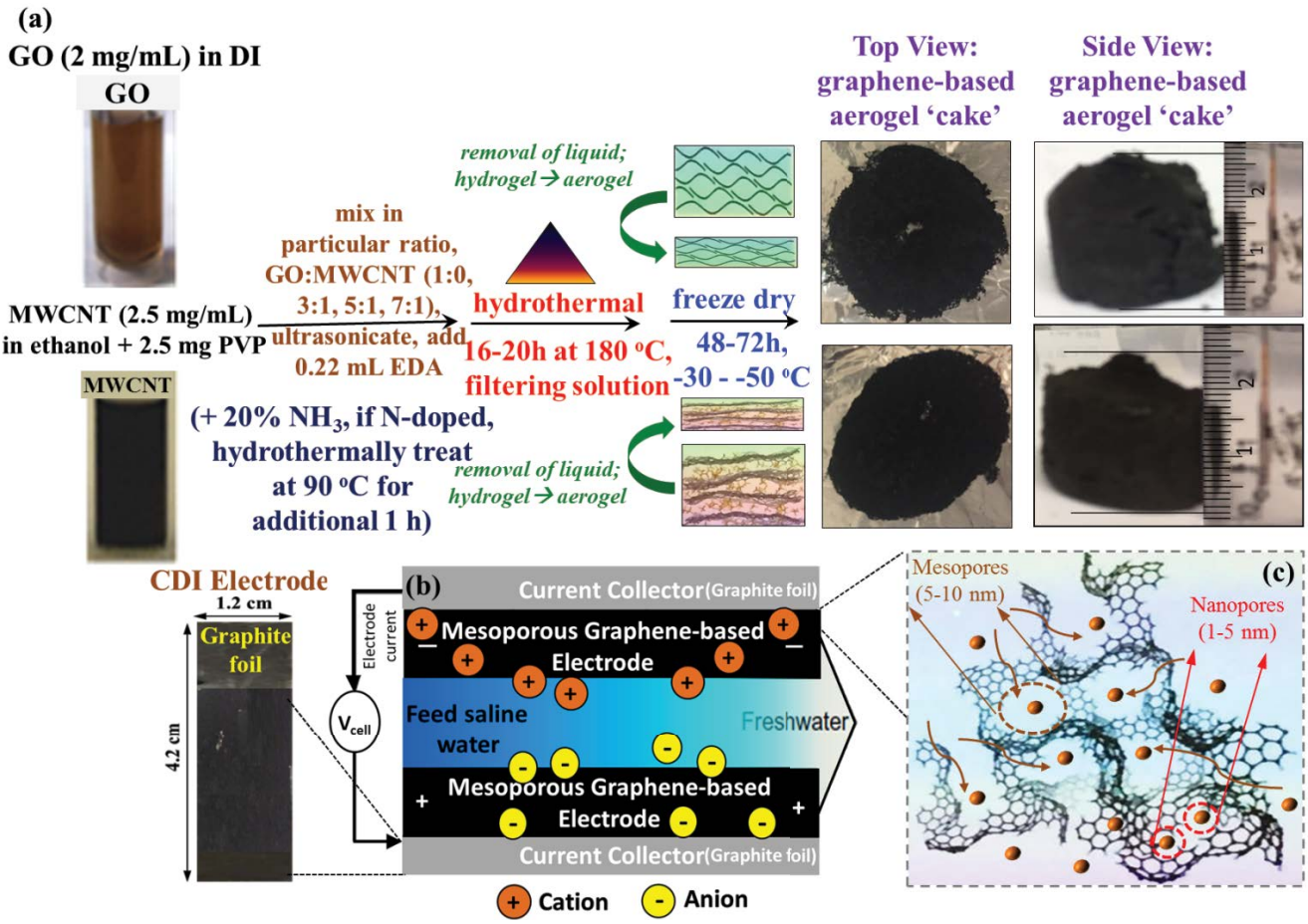

Fig. 1. (a) Schematic illustration of hydrothermal synthesis scheme of graphene-based 'hybrid' aerogels, (b) CDI electrode assembly and CDI process flow through mode, and (c) cartoon of GA with interconnected nanosheets.

of CDI electrodes based on these designer nanomaterials structures taking advantage of small diameter MWCNTs as viable 'spacers' for enhanced specific area from GNS. It is believed that the topologically interconnected mesopores and nanopores within graphene and graphene-carbon nanotube networks tend to enhance desalination performance by buffering ions shortening solid-state diffusion distance from external saline solution from brackish and seawater to the interior and exterior surfaces and interfaces. Furthermore, the exposed areas from nanopores edge sites can enlarge the surface area and hence augment both the electrosorption capacity and ion transport (Fig. 1). As expected, an ultrahigh electrosorptive capacity of 20.1-22.5 mg g^{-1} at a cell potential of 1.8 V is achieved, which is among the best performance reported for graphene-based CDI electrodes. We also compared the results with precursor GO film and thermally reduced GO (rGO_{th}) and holey graphene (hG) as well as nitrogen-doped Gr-MWCNT aerogels, which demonstrates the multiple roles of interconnected porous network and oxygenated (carbonyl; C=O, carboxyl; –COOH), and nitrogenated (pyridinic–N and pyrrolic–N) surface functional groups in enhancement of water desalination. Finally, we performed density functional theory (DFT) calculations that elucidate the finite electronic density of states (DOS) near Fermi level emphasizing defect-induced (e.g., vacancy) and heterogeneous atom (e.g. nitrogen or oxygen) binding sites improvements in physicochemical properties including heterogeneous electron transfer rate and ion transportation.

2. Experimental

2.1. Materials and methods

2.1.1. Preparation of graphene-based 'hybrid' aerogels and holey graphene

GAs were created using a scheme shown in Fig. 1a. This involves preparing two separate dispersions including multi-walled carbon nanotubes (MWCNT, diameter 8–10 nm) in ethanol at 2.5 mg/mL concentration by ultrasonication for 4 h and adding a small amount (2.5 mg) of PVP (polyvinylpyrrolidone) as the surfactant. The second dispersion is to prepare solution of graphene oxide (GO) prepared using modified Hummer's method with 2.0 mg/mL concentration in deionized (DI) water that is also ultrasonicated for 4–5 h. These dispersions were mixed together in varying ratio of GO and MWCNTs to create an array of aerogel with ratio 3:1, 5:1, and 7:1, respectively. A small amount of 0.56 mL of EDA (ethylenediamine) was added

for crosslinking GNS to carbon nanotubes. This solution was stirred to homogenize and then heated in autoclave at 180°C for 16–18 h. The dispersions were created with only MWCNT and GO also for comparison. Some of that GO dispersion was then nitrogenated by adding 13.4 mL of ammonium hydroxide (NH_3OH) to each 70 mL of solution (~20% ratio). This solution was heated in autoclave at 90°C for 1 h. These hydrogels with and without nitrogen were then freeze-dried for 6,072 h to remove water and create a range of aerogels.

2.2. Characterization

2.2.1. Morphology, microstructure, and electrochemical properties

All the samples were characterized using complimentary analytical techniques to reveal surface morphology, microstructure, and lattice vibration properties. Scanning electron microscopy (SEM) images were taken with an instrument (Model JSM-6510LV, JEOL Ltd. Peabody, MA, USA) operating at a primary electron acceleration voltage (V_{acc}) of 10–20 kV at constant current 45 μA in secondary electron imaging mode with a LaB_6 filament. For transmission electron microscopy (TEM), a few flakes were distributed onto commercial lacey carbon coated Cu grids (Ted Pella Inc., CA). TEM images were taken using a JEOL instrument (Model 1400 Plus, OR) operating in cryo-EM and SAED modes at 100–120 kV and 1 nA from LaB_6 gun with a Be specimen holder, a Gresham SiLi detector with Moxtek AP3.3 window and with AMT 8 Mpixel cooled camera. For SAED patterns, we used 0.10 mm aperture producing a small spot size. For electron tomography, single axis tilt-series are collected and processed using "SerialEM" IMOD and eTomo software (developed by the University of Colorado, Boulder, CO). The tomography software is fully integrated with an 8 M pixel AMT bottom mounted digital camera. TEM measurements provided nanoscale morphology and structure that help to determine inter-planar spacing and tomography for capturing three-dimensional hierarchical mesoporosity. Raman spectra were measured to determine carbon bonding phases. Raman spectra were acquired using a micro-Raman spectrometer (Model InVia Renishaw plc, Hoffman Estates, IL, USA) equipped with a laser providing excitation wavelength 633 nm (or energy 1.92 eV). The reflected light is filtered using an edge filter to remove the laser excitation cutting at ~100 cm^{-1} and sent to the spectrometer. The scattered light from the sample is collected in backscattering geometry transmitted and detected by CCD camera. An objective lens of 50x was used providing a spot size of ~1–2 mm and the laser power on the sample is maintained between <0.1 and 0.5 mW (1% or 5%) using neutral density filters to avoid local heating effects preventing photothermal degradation. The Raman spectra were acquired from 120 to 180 s depending upon the laser power used and to maximize throughput signal. Raman spectra ranged from 1,000 to 3,200 cm^{-1} samples with spectral resolution 1 cm^{-1}.

A custom designed single compartment three-electrode electrochemical cell was used for electrochemical measurements, using an electrochemical workstation (Model CHI920D, CH Instruments, Austin, TX, USA) in cyclic voltammetry (CV) mode, where the three electrodes included a Ag/AgCl reference electrode, a Pt wire counter electrode and the aerogel samples as the working electrode. The samples were electrochemically characterized using CV in the same feed saline solution 0.5 g/L NaCl and 0.5 g/L $MgSO_4$ in the potential range –0.6 V to +0.6 V at various scan rates v = 5, 10, 20, and 50 mV/s. Scanning electrochemical microscopy (SECM) was performed to determine heterogeneous electron transfer rate (k_{ET}). SECM measurements included probe approach curves those are described elsewhere [23]. For preparation and characterization of 'holey' graphene (hG) sheets in detail [15].

2.3. Fabrication of CDI electrodes

Slices of graphene-based aerogels with a thickness of ~1.5 mm were first cut from the as-prepared cylindrical monoliths. Subsequently, the aerogel slices were placed on the graphite foil as electrode substrates, to some aerogels a few drops of organic solvent N-methyl pyrrolidone (NMP) was added and air dried and compressed using hydraulic press during which the squeezed water or organic solvent was removed by filter papers. The samples were kept under a ~200 MPa pressure for 60 s to form ~25 to 40 mm well adhered films on the graphite electrodes. The size of all the electrodes was 1.2 × 4.2 cm^2 and the weight of these electrodes ranged ~30 to 50 mg. The GO precursor electrodes were also prepared by coating a few layers of GO dispersion on graphite foil and air-dried or thermally annealed at ~200°C in vacuum oven for 1 h to produce rGO_{th} electrodes.

2.4. Electrosorption tests

The electrosorption–desorption measurements were conducted in a custom-made continuous recycling system including a CDI unit cell, conductivity monitor and current recorder (Fig. 7, panel a). During each of these experiments, the feed solution was continuously pumped by a peristaltic pump into a unit cell and the effluent returned to the feed tank. In a typical experiment, the brine solution was prepared using pure sodium chloride (NaCl) and magnesium sulfate ($MgSO_4$) with initial concentration of 500 mg L^{-1} or 0.5 g/L, corresponding to conductivity of ~900 to 1,000 mS. The volume and the temperature of the solution were maintained at 50 mL and 298°K, respectively. A direct voltage of 0.8–1.8 V with an interval of 0.2 V was applied on the CDI cell. The variations in current and ion conductivity were recorded independently and simultaneously. Nevertheless, when we also calculated ion conductivity using the following:

$$k_{ion} = G \times K_{cell} \tag{1}$$

where G is conductance and inverse of electrical resistance of solution between two electrodes and K_{cell} is cell constant that is the ratio of distance (d) between the electrodes to the area (A) of the electrodes [24]. It should be noted that the hydrolysis of water did not take place for the voltage higher than 1.2 V due to the existence of finite resistance in the whole circuit and over potential between the two mesoporous electrodes (symmetric or asymmetric). We have also tested

some of the aerogels for seawater (source, Rehoboth Beach, Delaware-Atlantic Ocean) desalination.

3. Results and discussion

3.1. Phase morphology control and internal structure

An array of graphene-based 'hybrid' aerogels with tunable pore density are prepared by a one-step facile hydrothermal approach (Fig. 1a) which first produces graphene hydrogel (jelly-like macroporous material with high water content) in a Teflon-lined sealed autoclave, followed by freeze-drying that removes excess water molecules and yields a preserved hierarchical porous structure (Fig. 1b). Under hydrothermal conditions, nanoscale pores are generated in the basal plane of reduced graphene oxide basal plane where carbon atoms were etched and gradually extending pores from nanometer and sub-micrometers (mesopores) to several micrometers (Fig. 1c) and the chemical used result in high chemical surface charge. Figs. 2a and b show SEM and TEM images revealing the surface morphology and internal structure of freeze-dried Gr-MWCNT aerogels beside component aerogels and raw precursors (GO and rGO_{th}). The rGO sheets are topologically multiplexed with porous MWCNTs body to form a highly complex porous 3D network with well-defined pores. The high-magnification SEM and TEM images clearly indicate that the obtained 3D monolith 'hybrid' aerogels are composed of few-layered GNS interlinked through nanotubes. Furthermore, TEM and representative dual-axis tilt electron tomography (Fig. 2c) studies for we will perform dual-axis tilt electron tomography for three-dimensional reconstruction from processed projection images confirm the presence of abundant in-plane pores with nanometer and micrometers distributed over the entire GNS. In contrast, the precursors demonstrate smooth graphene morphology with only wrinkled and/or folded sheets. Hence, it is anticipated that the interconnected macroporous materials favor for large surface areas and optimize the porous structure maintaining structural integrity, which are desirable for high-performance CDI process and other relevant physical–chemical properties. Fig. 2b shows selected-area electron diffraction (SAED) patterns for GA, NGA, Gr-$MWCNT_{7:1}$, and Gr-$MWCNT_{3:1}$. The ring intensity patterns are labeled using Miller-Bravais (hkl) indices, that is, (100), (110), (002), and second-order (004). The presence of these rings indicates the medium-range order of all the graphene-based aerogels regardless of composition. The energy-dispersive X-ray spectroscopy (EDX) spectra (not shown) yielded C to O and C to N ratios 55.34–69.27 at.% and 75.34–89.27 at.%, respectively. In general, the findings from TEM in conjunction with SAED and tomography are strongly correlated. For holey graphene (hG), which is a nanomesh and a structural derivative of graphene clearly show an in-plane nanosize (2 nm for hG_1 and 5 nm for hG_{10}) circularly shaped holes. The hG was formed by removing significant number of carbon atoms from nanosheets leaving atomic scale vacancies that form nanopores on subsequent fusing of vacancies or carbon causing silver metal catalyst of two sizes leaving holes with size proportional to the size of the 'aggregated' catalyst particles apparent in Fig. 2b. These holes (or nanopores) are usually associated with abundant oxygenated and nitrogenated functional groups around their edges, on the protruded nanowalls and basal planes [21,25]. We have investigated the surface characteristics for the fabricated electrode materials by observing the static contact angles at room temperature qualitatively. From the static contact angle of a water droplet, the pristine thermally reduced graphene oxide surface appeared to be hydrophobic as compared with those graphene-based hybrid aerogels that showed considerable change in the droplet angle toward hydrophilicity. Therefore these surfaces showed considerable wettability behavior without pore blocking that should lead to an enhancement in specific adsorption rate from saline solutions to the electrode surface.

Fig. 3 shows representative XRD patterns for GO, GA, Gr-$MWCNT_{5:1}$, NGA, and N-Gr-$MWCNT_{5:1}$ aerogels. GO exhibits a distinct peak centered at $2\theta = 13.3°$ (001) and graphitic peak typically occur at 25.5°–26° (002) confirming the large interlayer spacing of GO owing to abundant water molecules and oxygen-containing groups. After reduction, aerogels show the characteristic GO peak upshifts and a broad (002) peak indicating reduction of oxygenated functional groups. N-doped aerogels also show the same behavior with marginal reduced intensity possibly due to dislocation of stacked GNS or loosely stacked GNS and nitrogenated graphene-based aerogels showed a sharper peak at around 26.1°. The microstructural changes during hydrothermal chemical processing from pristine GO and rGO following aerogels formation, their nitrogenated analogs and hG, are also reflected in Raman spectra shown in Fig. 4a. The Raman spectra display prominent G peak which is broadened and shifted to 1,594 cm^{-1} (ca. 1,581 cm^{-1} for graphite and arises due to zone center phonon with E_{2g} symmetry) and D band (arises due to the breathing mode of k-point phonons of A_{1g} symmetry) at ~1,350 cm^{-1}. The G band originates from in-plane vibration of sp^2 bonded C atoms and D band is Raman-forbidden and usually disorder activated. Other bands are second-order D band (2D), a combination D + G band and second-order G (2G) band at approximately 2,680⁻; 2,920; ⁻and 3,180 cm^{-1}, respectively. For a realistic comparison, all the Raman spectra are normalized to G band. Qualitatively, while relatively narrow G band indicates structural or crystalline order, the presence of a finite D band originates from the large density of defects (edge sites, grain boundaries, vacancies, substituted heteroatoms) for all the graphene-based aerogels and holey graphene (hG_1 and hG_{10}) samples characterized. It is worth mentioning that there is a disorder-induced signal D′ band occurring at 1,620 cm^{-1} for GA, NGA, NFG, Gr-$MWCNT_{5:1}$, and hG_{10} the origin of which is yet to be established. Moreover, the D peak is not sensitive to the defect geometry, but only to the amount of disorder [26]. Fig. 4b summarizes the structural evolution in the Raman spectra for all the samples prior to and post mesoporous graphene formation and there are several noteworthy features where the results are in agreement with literature reports [26–28]. The D band position (w_D) decreases with addition of MWCNT from 1,340 to 1,330 cm^{-1} for all of the aerogels studied in this work and almost comparably higher (1,345 cm^{-1}) for holey graphene (hG_1 and hG_{10}) as compared with GO and rGO (1,350 cm^{-1}) precursors used to prepare them. On the other hand, G band position (w_G) marginally

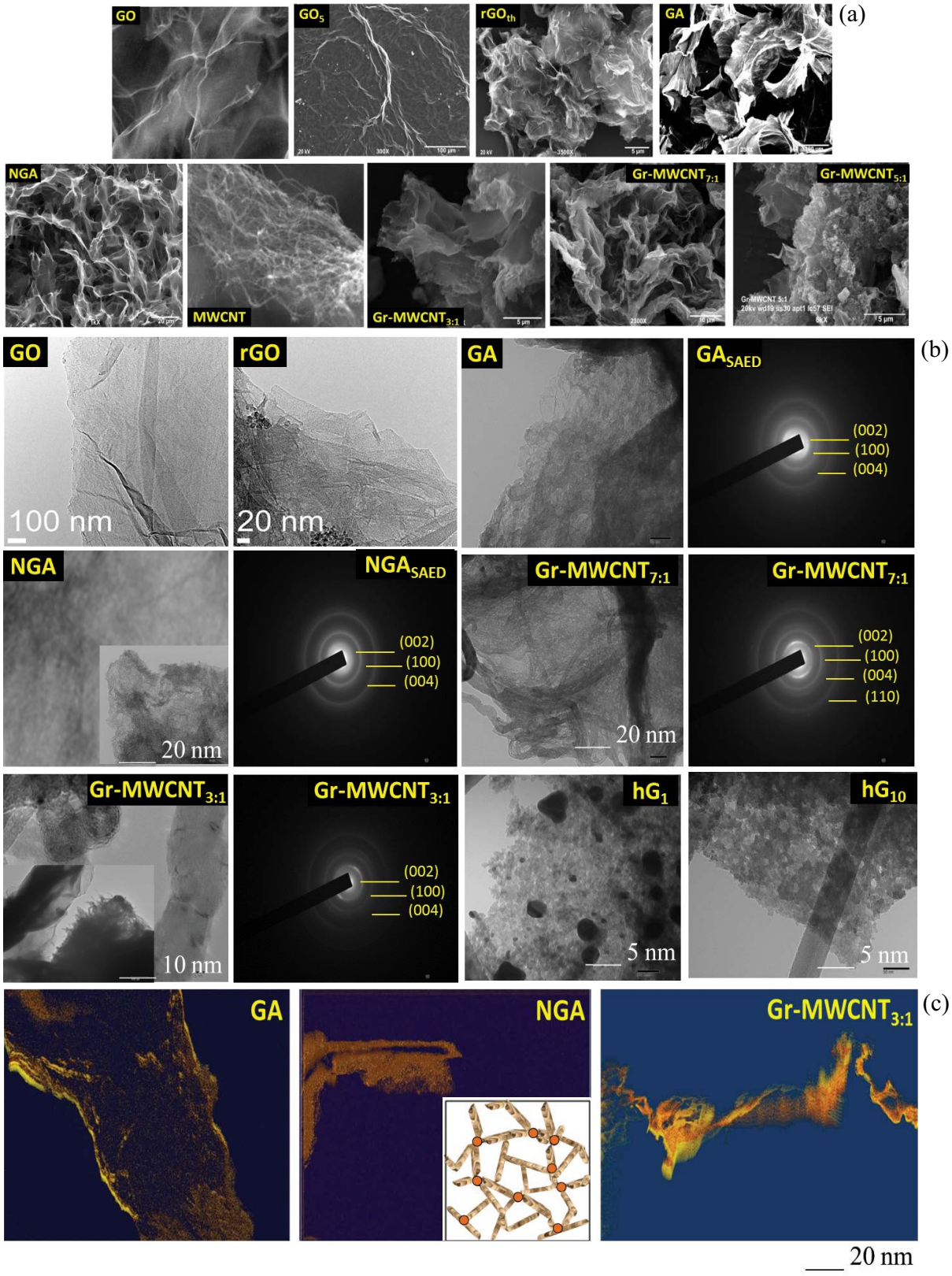

Fig. 2. (a) SEM and (b) TEM with selected-area electron diffraction images of freeze-dried graphene-based aerogels and holey graphene (hG_1 and hG_{10}) revealing morphology and internal microstructure besides graphene precursors and nitrogenated graphene aerogel (NGA), (c) Representative electron tomography of GA, NGA and Gr-MWCNT$_{3:1}$ 'hybrid' aerogels showing nanoporosity (Scale bars are shown at the bottom of the images and inset: a cartoon schematic of interconnected porous GNS networks with node points).

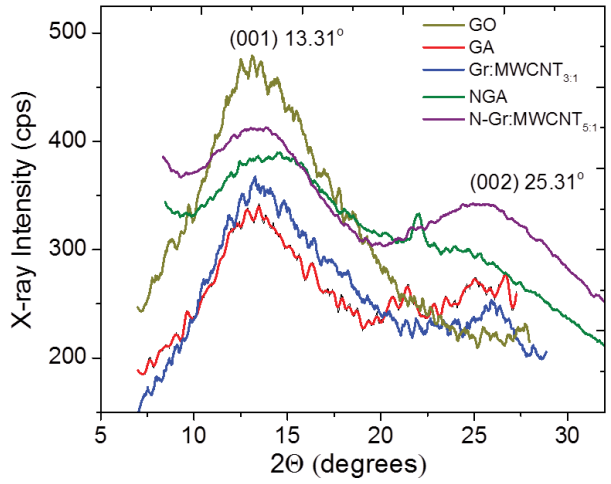

Fig. 3. Representative X-ray diffraction of the synthesized aerogels as CDI electrode materials and GO precursor.

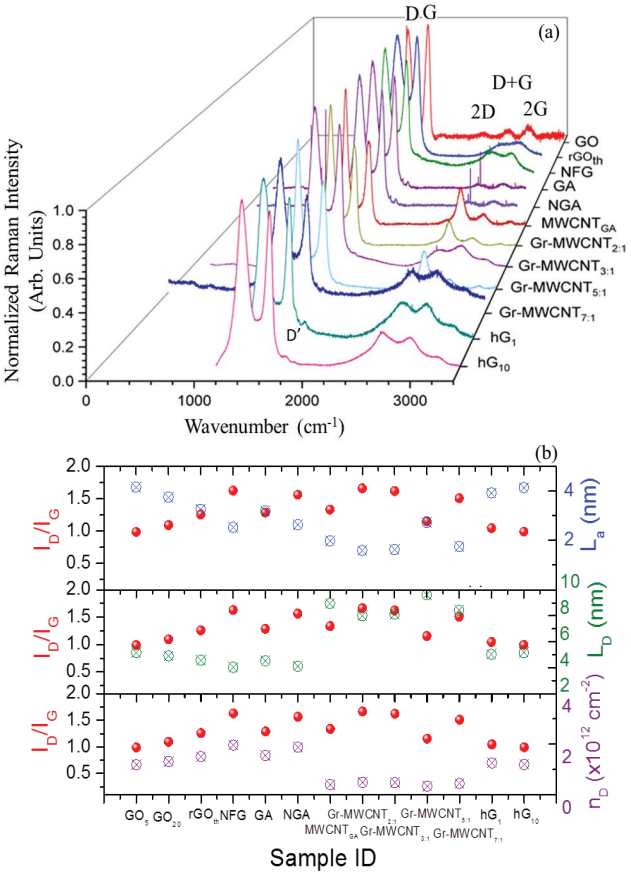

Fig. 4. (a) Micro-Raman spectra of precursors GO, rGO_{th}, graphene-based 'hybrid' aerogels, NGA and holey graphene showing first-order prominent D and G bands, second-order 2D and 2G bands and combination D + G band and (b) variation of Raman spectral bands in terms of intensity ratio of D to G band (I_D/I_G) and corresponding in-plane sp^2 C cluster size (L_a, nm), defects domain distance (L_D, nm) and number defects density (n_D, cm^{-2}).

increases from 1,586 to 1,596 cm^{-1} for both the GAs and holey graphene. It is well documented that the intensity ratio of D to G band (I_D/I_G) is a semi-quantitative measure of structural order (Fig. 4b). Under the assumption, the defect density is sufficiently lower than critical concentration, the D band intensity is proportional to the number density of point defects (n_D) and the average inter defect distance (L_D), not the nanocrystallite size L_a, that is, in-plane sp^2 C clustering size and a larger intensity ratio mean smaller sp^2 C domains, determined using Tunistra-Koening (T-K) relation [29]:

$$L_a(\text{nm}) = (3.84) \times \left(\frac{I_D}{I_G}\right)^{-1} \tag{2}$$

A quantitative formula is typically used to correlate the mean distance between defects (L_D, nm) in graphene with the intensity ratio of I_D/I_G [30,31]. The defect density n_D (cm^{-2}) is then given as follows:

$$n_D = \frac{10^{14}}{\pi L_D^2} \tag{3}$$

Both L_D and n_D have been used to quantify the defect density in these graphene-family nanomaterials. We note that for all aerogels, the I_D/I_G increases as compared with GO and rGO and this change suggests a decrease in the average sp^2 C domains/cluster size upon reduction and transformation to GAs. It can be explained as if new sp^2 C domains smaller in size albeit more in number are created to those present in raw precursors. The ratio I_D/I_G reaches a maximum ~0.5 to 2.0 yielding average L_a ~2 to 5 nm size and an inter defect distance L_D ~2 to 10 nm depending upon the GA. With further increase in defect density, the activated area coalesce and the "structurally disordered' area dominate in the graphene sheet, which leads to decrease in D band intensity. The defect number density, n_D values ranged between 1 and 4 × 10^{12} cm^{-2} summarized in Fig. 4b, which is much smaller than the wholly disordered graphene with 10^{15} cm^{-2} defects meaning one defect per three to four carbon atoms [32].

3.2. Electrochemical characteristics of fabricated electrodes

Based on electrochemical double layer capacitor (EDLC), CV measurements are widely used as an effective and reliable way to determine the electrosorption ability and specific capacitance of electrode materials. It is noteworthy to mention that the electrochemical results were obtained under the same condition of NaCl and $MgSO_4$ concentration as of the CDI process: with two working electrodes in symmetric configuration separated by a separator. Fig. 5a shows representative CV curves of symmetric electrodes made with NGA and NMP for consolidating the aerogels without any binder on graphite foil, at scan rates 5, 10, 20, and 50 mV/s in 0.5 g L^{-1} NaCl and $MgSO_4$ electrolytes. No Faradaic peaks are present in any of the CV profiles for all of the materials (not all of them are shown); this reflects the adsorption of ions on the surface of mesoporous graphene-based aerogels based on Coulombic interactions rather than redox reactions.

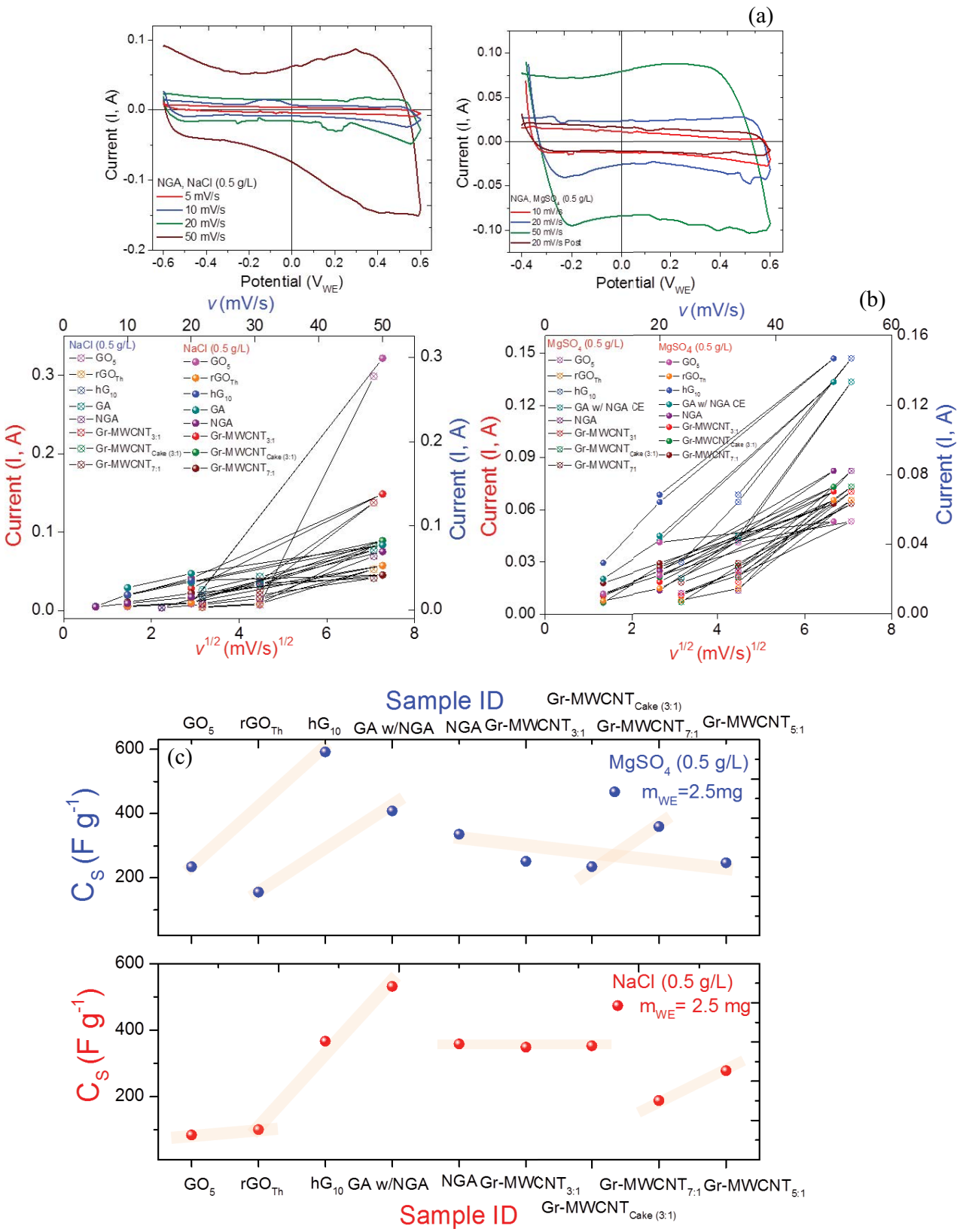

Fig. 5. Representative (a) cyclic voltammograms of NGA as CDI electrodes at various scan rates, 5, 10, 20, and 50 mV/s in test saline solutions (0.5 g/L NaCl and $MgSO_4$), (b) Variation of peak current with scan rate and (scan rate)$^{1/2}$ for all the aerogels as CDI electrodes besides graphene precursors, and (c) Specific capacitance for all the aerogels tested in 0.5 g/L NaCl and $MgSO_4$.

Most of the traces are clearly symmetric with respect to the X-axis or abscissae with ideal rectangular shape, reflecting typical electrochemical double-layer capacitance and a highly reversible capacitive process. The graphene-based hybrid aerogels (e.g., Gr-MWCNT$_{5:1}$), nitrogenated aerogels and hG$_{10}$ exhibit greater accessibility to storage ions as compared with others. We have also prepared two asymmetric cells combining Gr-MWCNT$_{3:1}$ and hG$_{10}$ and GA and NGA and to our surprise they exhibited the best electrochemical performance. It can be attributed to the capabilities of asymmetric functional groups (–C–N) and (–COO) of electrodes to reduce co-ion expulsion similar to the role of membrane for blocking co-ions from carrying parasitic current and hence enhance the adsorption capacity of the electrode assemblies. The variation of current with scan rate and square root of scan rate is plotted in Fig. 5b and specific capacitance (C_s) values plotted in Fig. 5c have been calculated from CV results according to the following equation:

$$C_S = \frac{\bar{I}}{vm}\left(\mathrm{F.g^{-1}}\right) \tag{4}$$

where $\bar{I}$ is the average current (A), v is the applied scan rate (V/s) and m is the mass of the active electrode material (g). The Gr-MWCNT$_{3:1}$ and hG$_{10}$ have the highest specific capacitance followed by Gr-MWCNT$_{5:1}$, NGA and Gr-MWCNT$_{5:1}$ aerogels indicative of optimized morphology and microstructure. Interestingly, there is also an interplay of oxygenated and nitrogenated surface functional groups and hierarchical porosity which showed significant improvement in specific capacitance (C_S) compared with symmetric GO and rGO raw precursors due to decreased graphene polarization and enhanced ion selectivity. The analysis of reversible current helps to determine diffusion coefficient (D) governed by the Randles–Ševćik equation:

$$I_{\mathrm{rev}} = (2.69\times10^5)n^{3/2}ACD^{1/2}v^{1/2} \tag{5}$$

where A is the geometric area of the electrode (cm^2), F is the Faraday constant (C mol^{-1}), D is the diffusion coefficient (cm^2 s^{-1}), C is the concentration (mol/cm^3), v is the scan rate (V s^{-1}), R and T are usual constants, and n is the total number of electrons transferred in the electrochemical process [4,33,34]. The diffusion coefficient (D) ranged between 1.5 × 10^{-9} and 6.7 × 10^{-8} m^2 s^{-1} following the order GO < rGO$_{th}$ < hG$_{10}$, < GAs ≤ nitrogenated GAs, respectively. An increase in D values for GAs is attributed to surface morphology and nanoscale pore size distribution at meso/nanoscale, thus permitting access to numerous hydrophilic edges, surface functional groups as well as basal plane defects sites. These CDI electrodes also exhibited high electrical conductivities (≥10^2 S/m, Fig. 6), relatively low internal and charge transfer resistance of ≤10 W and ≤5 W determined from impedance spectroscopy (Fig. 6) and large internal surface areas (≥600 m^2/g) thus enhanced ion storage capacity compared with those with physical cross-linked porous structures (≤1 S/m).

3.3. Desalination performance and electrosorption capacity

Prior to conducting experiments to estimate the adsorption capacity of the fabricated aerogel electrodes, all the electrodes were activated by soaking in 0.25 g L^{-1} NaCl or $MgSO_4$ solution for 10 min. under vacuum to remove any air bubbles. A typical CDI flow-through system consists of a reservoir, peristaltic pump, CDI unit cell, and conductivity meter (Fig. 1a) [35]. A pair of electrodes was assembled in a prototype CDI cell as in Fig. 1b. The CDI unit cell is composed of two parallel similarly prepared CDI electrodes separated by a non-conductive spacer (nylon cloth, 125 mm thick). The test salt solutions are continuously pumped into the CDI cell at 20–30 mL min^{-1} with an initial conductivity approximately 800–900 mS using a single-pass method. The CDI tests were conducted in NaCl and $MgSO_4$ aqueous solutions with concentration 0.5 g L^{-1} at different applied voltages from 0.8 to 1.8 V with interval of 0.2 V. We have also attempted to desalinate actual ocean water with initial conductivity of 415 mS in an asymmetric CDI cell consisting of rGO$_{th}$ and hG$_{10}$. In a typical electrosorption-desorption cycle, a certain cell voltage is applied across electrodes for a period of time before it is shorted. The corresponding current response for electrodes and the conductivity of testing salt solutions were recorded simultaneously and independently. Figs. 7a–d shows the change in current (and conductivity) profiles of effluent during adsorption/desorption process for representative electrodes and under cell potential from 0.8 to 1.8 V. Apparently, the detected current rapidly decreases particularly for mesoporous electrodes beyond 1 V of the external potential during adsorption step, suggesting an onset potential and indicates removal of the salt ionic species on the oppositely charged electrodes due to adsorption. With progress in time, and higher potential of 1.6 or 1.8 V, the rate of adsorption of ions represented through current or conductivity curves persistently becomes slow because of saturation of the adsorption capacity of the electrodes and finally attains an equilibrium or adsorption plateau. In other words, the electrostatic repulsion between the adsorbed ions and solution ions occurred. Fig. 7e summarizes the change in conductivity (experimental and calculated) as histogram from feed to electrosorbed solution at 0.8 and 1.8 V for all the electrodes tested including control and/or precursor films. Apparently, it shows that the conductivity descended with the large change observed for binder-free Gr-MWCNT$_{5:1}$, MWCNT$_{aero}$, NGA, GA, and hG$_{10}$ electrodes and for the remaining electrodes the change was intermediate. For ocean water test, the conductivity change was 25% only in one cycle with hG$_{10}$ electrode which demonstrates promise for sweater desalination with moderate efficiency. Besides lowering conductivity, compared with precursor GO film, the composite aerogel electrodes required a relatively longer time to be saturated meaning more adsorption of ions on the electrode surface thus more energy efficient. It is worth mentioning, the sharp increase in conductivity at desorption stage corresponds to the expulsion of ions adsorbed at reverse current under 0 V. This indicates that desorption process is faster and easier for aerogels than GO$_{film}$ precursor thin films. In addition, conductivity variations are reproducible for several cycles of electrosorption and desorption, indicating good regeneration of electrodes which are important factor for evaluating the cost effectiveness, energy efficiency, and reliability of the CDI electrodes.

Note that the salt removal or electrosorption capacity (Q, mg g^{-1}) and the rejection efficiency (h_d) of the electrodes

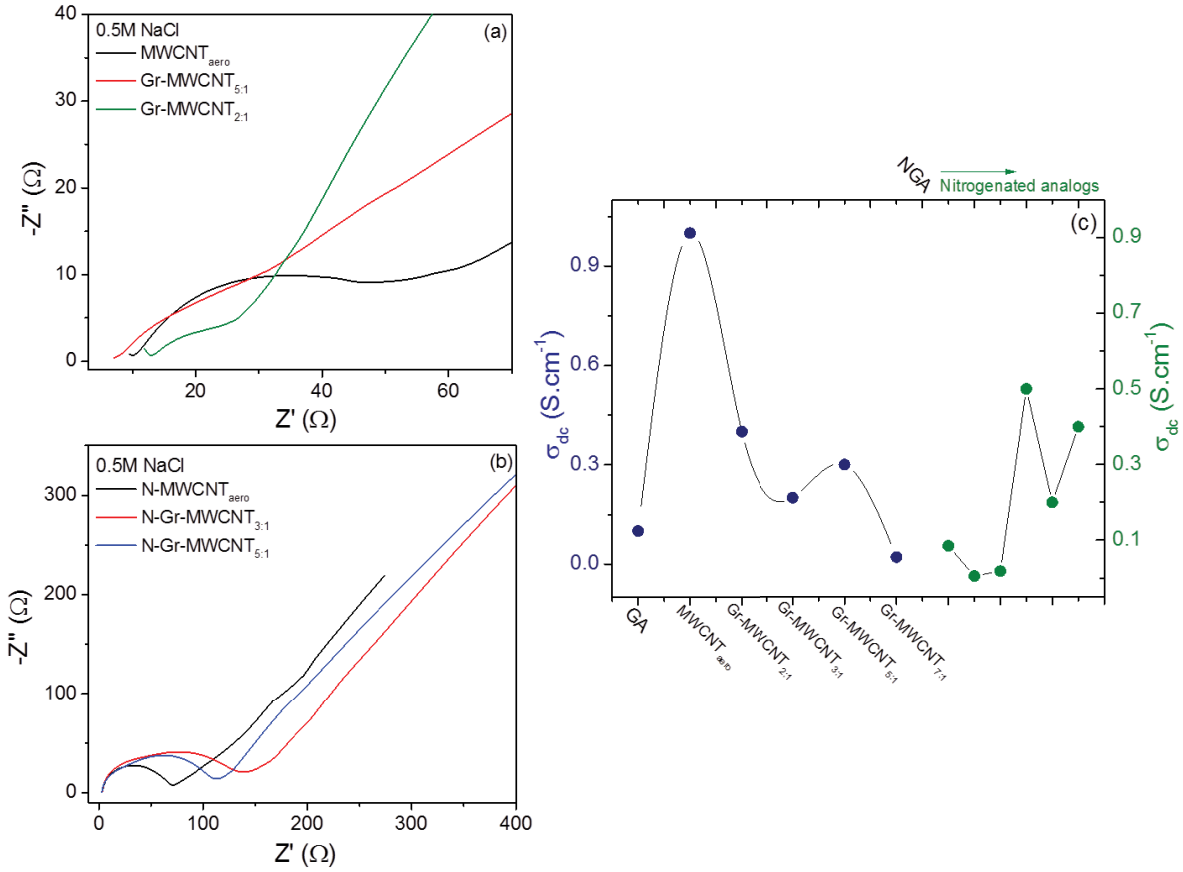

Fig. 6. Representative electrochemical impedance spectroscopy (EIS) Nyquist plots for (a) $MWCNT_{aero}$, $Gr\text{-}MWCNT_{5:1}$, $Gr\text{-}MWCNT_{2:1}$ and (b) $N\text{-}MWCNT_{aero}$, $N\text{-}Gr\text{-}MWCNT_{3:1}$, and $Gr\text{-}MWCNT_{5:1}$ aerogels. The room temperature DC electrical conductivity (s_{dc}, S cm^{-1}) of all the aerogels studied.

were exactly calculated based on newly presented integration equations rather than conventionally used equations [15]:

$$Q = \frac{\left[\int_{t_0}^{t_s}\left(\frac{C_0 - C}{t}\right)dt\right] \times v \times \left(t_s - t_0\right)}{M} \tag{6}$$

and

$$\eta_d = \left[\int_{t_0}^{t_s}\left(\frac{C_0 - C}{C_0 t}\right)dt\right] \times 100 = \frac{Q \times F}{\Sigma} \tag{7}$$

where C_0 (mg L^{-1}) is the initial concentration of NaCl or $MgSO_4$, C is the concentration of the effluent solution at time t of NaCl or $MgSO_4$, v is the volumetric flow rate (L s^{-1}), M (g) represents the mass of the carbon electrodes, S (C g^{-1}) is obtained by integrating the corresponding charging current, F (96485 C mol^{-1}) is Faraday constant, t_0 and t_s are the initial and saturated time, respectively. Using the new equation considering all important variables, the electrosorption capacity was determined that ranged approximately from 4 to 22 mg g^{-1} compared with various electrodes in Figs. 8a and 8a' with applied voltages and it follows GO_{film} < $MWCNT_{aero}$ < GA < NGA < $Gr\text{-}MWCNT_{5:1}$ order. Typically, the adsorption capacity of all of the electrodes increases with applied voltage and adsorption capacity of mesoporous composite electrodes is much higher than those of GO_{film}. The excellent deionization or ion adsorption capacity can be attributed to decrease in electric polarization and surface wettability in addition to rapid and easy adsorption for ions via intra-channel pathway accompanied by accessibility of electrodes surface through topological network of GNS that are chemically bridged through nanotubes. Charge efficiency is another functional parameter to gain insight into the double layer formed at the interface between electrode and solution which is calculated using the above-mentioned equation. Fig. 8b shows the charge efficiencies (i.e., the ratio of equilibrium salt adsorption over charge) variation with applied voltages for all the representative electrodes. Higher charge efficiency of graphene-based 3D scaffold as compared with thin films is attributed to their surface morphology and interconnectedness with hierarchical porosity which facilitates faster ion diffusion and charge transfer. These findings will be supported through advanced electrochemical characterization below. Inspired by Ragone charts typically used to represent energy storage devices with specific and volumetric power vs. energy density, one can determine

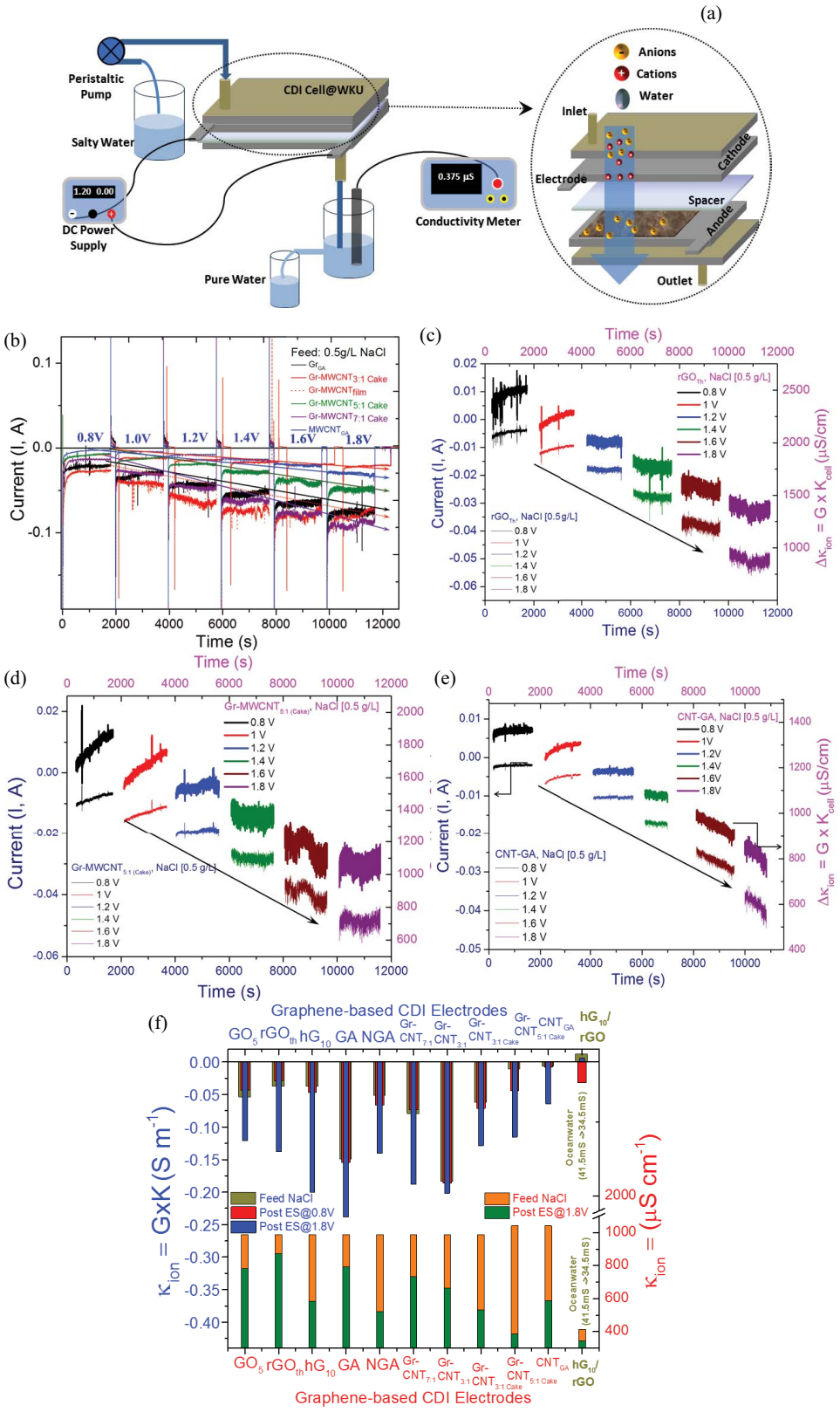

Fig. 7. (a) Experimental schematic of the capacitive deionization setup in flow-through mode. The electrosorption–desorption performance in terms of, (b) current response for various aerogels and, (c–e) ion conductivity change (Dk_{ion}) for rGO_{th}, Gr-$MWCNT_{5:1}$ and CNT-GA (or $MWCNT_{aero}$) in 0.5 g/L NaCl feed solution with varying cell voltage from 0.8 to 1.8 V, and (f) Histogram of ion conductivity k_{ion} (S m^{-1}) or (mS cm^{-1}) determined from experimental current response for all graphene-based nanomaterials and aerogels.

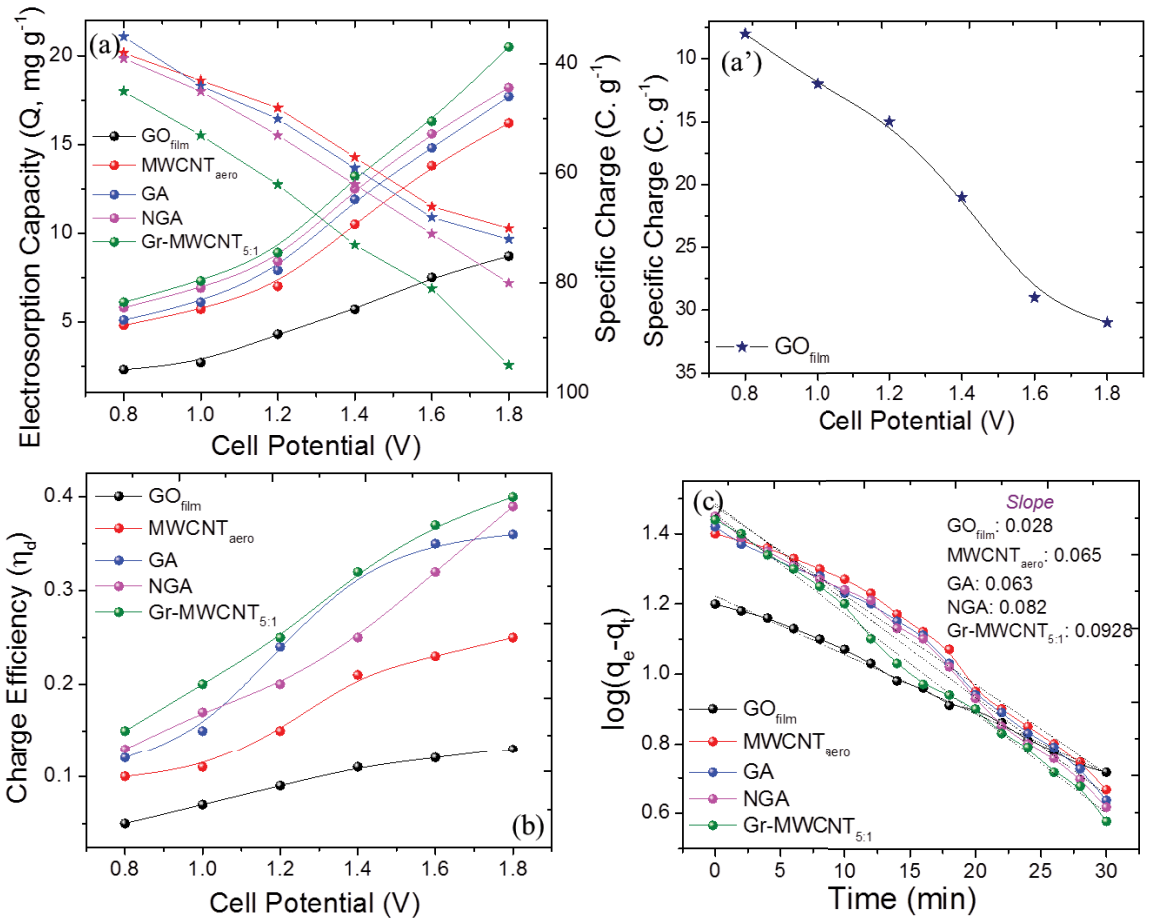

Fig. 8. (a) Removal capacity, (a') specific charge, and (c) charge efficiency, with respect to cell potential, and (d) electrosorption kinetics in 0.5 g/L NaCl at cell potential of 1.4 V, of precursor GO_{film}, $MWCNT_{aero,}$ GA, NGA, and Gr-$MWCNT_{5:1}$ aerogels as CDI electrodes.

optimal CDI cell operational conditions and unprecedented quantitative view when both these parameters attain maximum values. Another important characteristic of adsorbents is adsorption rate, often determined by Lagergren's pseudo-first-order adsorption kinetics [36]:

$$\log\left(q_e - q_t\right) = \log q_e - \frac{k_1 t}{2.303} \tag{8}$$

where q_e (mg g^{-1}) and q_t (mg g^{-1}) are the amount of salts adsorbed at equilibrium and time t (min), respectively. k_1 (mg g^{-1} min^{-1}) is the adsorption rate constants. Fig. 8c shows the linear fit between the experimental data and the equation above with average regression coefficient of 0.9944. The upper and lower bound rate constants k_1 determined from the slope of the fitting straight lines are ~0.10 and 0.028 for GO_{film} and Gr-$MWCNT_{5:1}$ composite aerogel, respectively, and all other materials values lies in-between. The high-rate constant for aerogels is ascribed to the high accessibility of electrodes surface, edge interfaces and defect sites to charged species. It is noted that efficient electrosorption and desorption is desirable for practical CDI devices to ascertain maximal desalination producing clean water.

While we have performed extensive characterization of CDI electrode materials, we have also determined electron transfer rate (denoted as k_{ET}) using SECM technique [25]. Fig. 9 summarizes the results and plots rate constant k_{ET} (cm s^{-1}) via SECM correlated with structural parameters (defects number density, n_D [cm^{-2}] and inter-defect distance, L_D [nm]) derived via Raman spectroscopy, for all the graphene-based aerogels. The data points in solid and hatched red circles are from the measurements with two polarities (alternatively, different complementary surface charge). The k_{ET} values ranged 4×10^{-2}–4.0×10^{-1} cm s^{-1} for all the electrode materials investigated within an accuracy ~0.1%, smaller than the typical experimental uncertainty. These are higher than those of values reported for pristine chemical vapor deposited graphene layers (2.0×10^{-2} –4.2×10^{-2} cm s^{-1}) in aqueous solution [37]. The difference is attributed to tunable morphology, structural quality, basal and edge site defects density in graphene-based aerogels. While correlating the k_{ET} with both n_D and L_D, the multi-compartment behavior corroborated with Raman spectral behavior for D-band results suggest that moderate defects density and a critical defect distance (or pore size) are necessary in acquiring enhanced electrochemical activity. The high k_{ET} values can also be related to high electrosorption

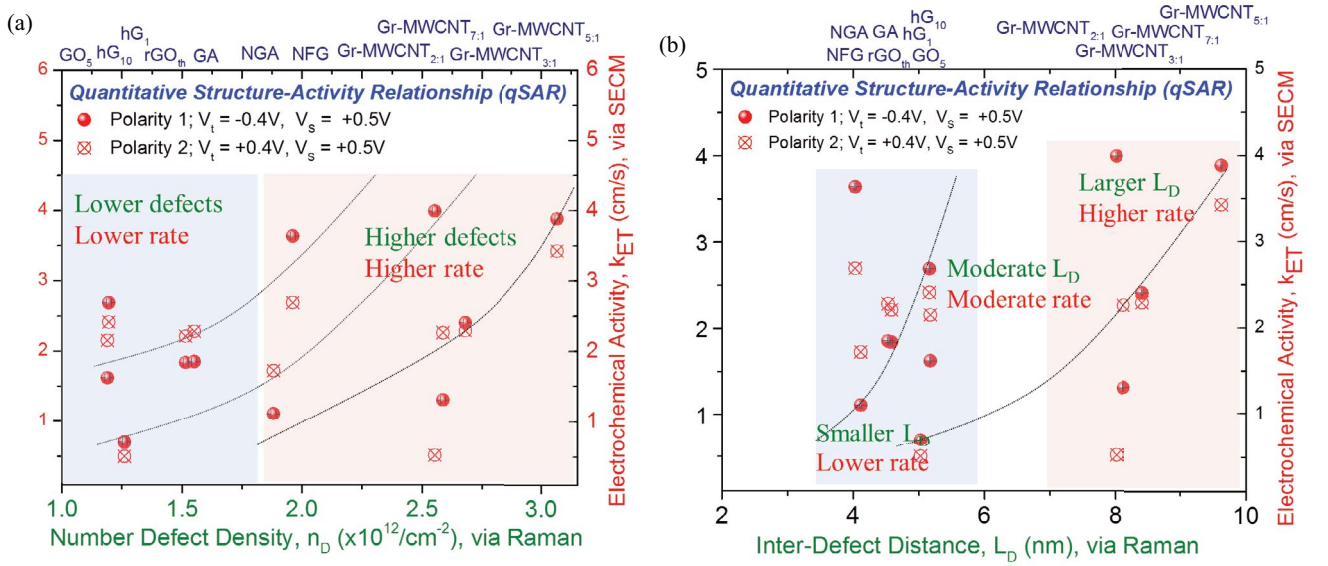

Fig. 9. (a) Defect density (n_D) (via Raman spectroscopy) [6] and (b) inter-defect distance (L_D) (both via Raman spectroscopy) correlated heterogeneous electron transfer (HET) rate constant (k_{ET}) (via SECM), for all the graphene-based aerogels. The dashed regions represent different regions and solid lines are a guide for the eye.

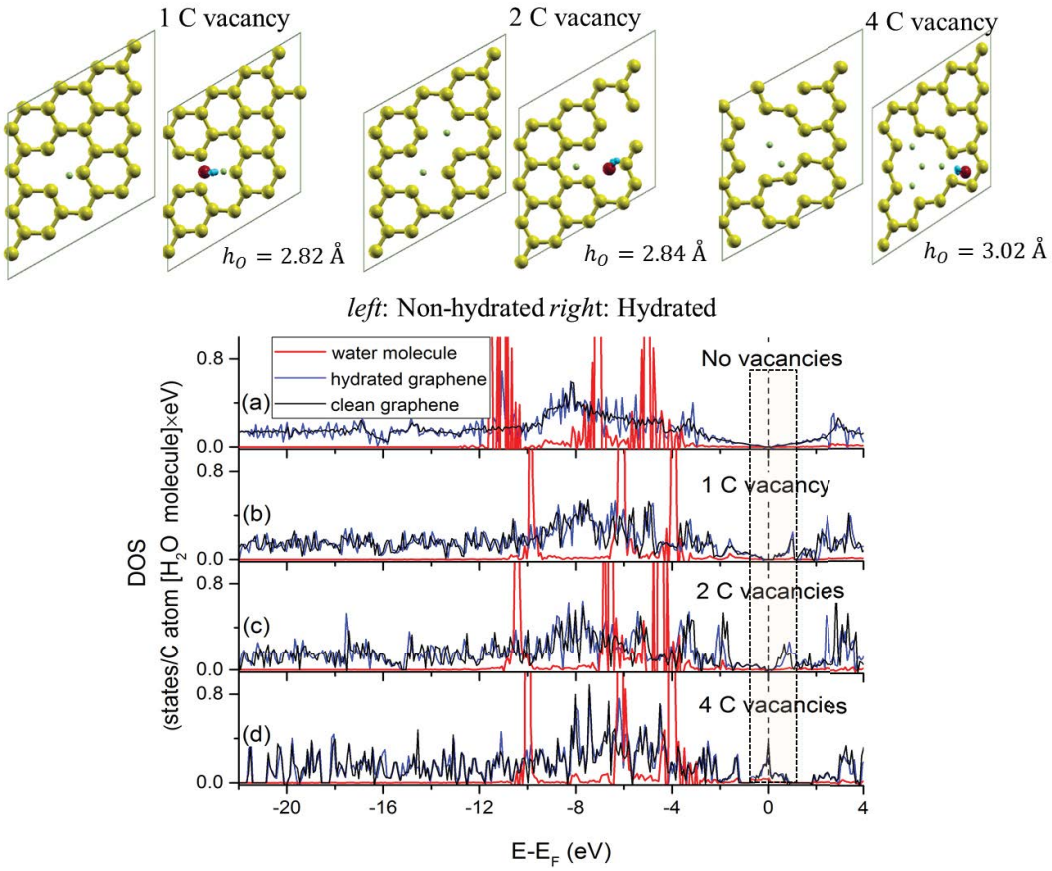

Fig. 10. DFT optimized geometries of hydrated and non-hydrated graphene layer with vacancies (adapted from ref. 40). For H_2O/graphene without defects, h_0 = 3.04 Å. Graphene DOS spectra per carbon atom for water/graphene and clean graphene systems and for the absorbed water molecule (a) without carbon vacancies, (b) with one carbon vacancy, (c) two non-adjacent carbon vacancies, and (d) four adjacent carbon vacancies. The vertical line is the Fermi level (E_F) indicates the increasing defects with vacancies thus increased C edge sites.

capacity. On theoretical consideration, the electron transfer kinetics is determined by the integration of electronic states of graphene material and the number of oxidized states of redox probe potassium ferricyanide, $K_3Fe(CN)_6$ near the Fermi level (E_F) for a reduction reaction [23,38]. Alternatively, the improved k_{ET} can be understood by the presence of finite and increasing electronic DOS in the vicinity of Fermi level (E_F). As a consequence, DOS was computed via DFT calculations in defective graphene (point defects or vacancies) with and without water molecules [23,39]. Fig. 10 shows optimized geometries and electronic DOS spectra of defective graphene with increasing vacancy (i.e., equivalently holey graphene with increasing pore size). With introduction of point vacancy defects, the defect induced localized midgap states with high DOS near Dirac point is observed. The latter enlarges the overlap between the GFNs and redox probe, which facilitates higher electron transfer rate from mesoporous graphene and probe molecule $K_3Fe(CN)_6$ on reduction. It was found that with increasing defect density, the graphene becomes fully activated for $L_D > 3$ nm, that is, outside the activated area. Indeed, we observed an enhancement of k_{ET}, corresponding. Note that the highest defect density in this study (4×10^{12} cm^{-2}) is lower than that of the fully disordered graphene, which has a defect density of 10^{15} cm^{-2} (i.e., one defect per four carbon atoms). Therefore, the improved electroactivity due to defects site density and surface redox chemistry due to groups (O and N) play a vital role and they are crucial for CDI and applied electrochemical applications [23].

Compared with reported graphene-based electrodes materials, our findings show either comparable or higher performance in terms of specific capacitance, electrosorption capacity and salt ion rejection efficiency. Therefore, the excellent desalination performance of these novel CDI electrodes is attributed to: (1) constructing 3D graphene-based architectures with carbon nanotubes as an effective approach to prohibit re-stacking GNS meanwhile enhancing high surface area of graphene and showing macroporous and hierarchical structure and complex morphologies, (2) the topologically interconnected pore network with graphene and nanotubes with enhanced interfaces which are favorable for buffering ions to shorten the diffusion length from test electrolytes to interior surfaces, and (3) thin lamellar walls or strut sizes of nanoporous graphene and hierarchical graphene-based aerogels which enhance the ion transportation and subsequent electrosorption capacity. Finally in the CDI process, smaller pores than a specific value (cutoff pore width) do not contribute to the total electrosorption capacity due to an overlap of electrochemical double-layers. The augmented effects are sufficiently evident in micro- and nanoporous 3D graphene-based CDI electrodes.

4. Conclusion

In conclusion, we have demonstrated an array of novel CDI electrodes design by creating three-dimensional graphene architectures using a facile hydrothermal approach. The three-dimensional monolith aerogels show (a) highly interconnected topological network of GNS with, (b) hierarchical in-plane porosity with uniform strut size having, (c) higher specific surface area, (d) good electrical conductivity, and (e) wettability, resulting in efficient salt ion electrosorption capacity and pathways for ion transportation which allowed achieving ultrahigh desalination performance during CDI process. An ultrahigh electrosorptive capacity 22 mg g^{-1} at cell potential 1.8 V was obtained with novel graphene-based aerogel electrodes. This could be attributed to the interconnected mesoporous network within the GNS and carbon nanotubes that allow larger accessibility for ion adsorption. The results elucidate the interplay of meso- and nanoscale porosity, aerogel struts with lamellae connected at nodes having large number of edge interfacial density, oxygen and nitrogenated surface functional groups that are favorable for significantly improved CDI performance, by buffering ions to reduce the diffusion distance from saline water to the interior surfaces of these 'hybrid' aerogels. Considering the availability, the proposed composite aerogels can be strongly recommended as cost-effective and efficient electrode materials for water desalination and generally for nanoionics. The results obtained in this study strongly suggest that mesoporous graphene-based materials and multilayer nanoporous hole graphene are superior for CDI water desalination. This is attributed to the fact that a large fraction of the carbon aerogel surface area comes from micropores that is not typically accessed by the adsorbing ions. This work indicates good promise toward implementation of mesoporous carbons as CDI electrodes at small-scale or portable desalination systems.

Acknowledgments

The author (S.G.) gratefully acknowledges financial support in parts by KSEF-RDE (Grant #148-502-17-397), KY NASA EPSCoR RIDG (NASA RID-3-NNX15AK28A, subaward# 3200000029-17-229), KY NSF EPSCoR REG (subaward# 323200000271-18-059), KY NSF EPSCoR RSP (subaward# 3200000271-17-212), NSF-MRI (Grant# 1429563), and NSF EPSCoR Track RII (subaward# EPS-0814194). The student co-authors (B.E., A.H.) are thankful to John Andersland (Biology) for SEM, TEM and electron tomography training.

References

[1] M.A. Shannon, P.W. Bohn, M. Elimelech, J.G. Georgiadis, B.J. Mariñas, A.M. Mayes, Science and technology for water purification in the coming decades, Nature, 452 (2008) 301–310.
[2] M. Elimelech, W.A. Phillip, The future of sweater desalination: energy, technology and the environment, Science, 333 (2011) 712–717.
[3] A.D. Khawaji, I.K. Kutubkhanah, J.-M. Wie, Advances in seawater desalination technologies, Desalination, 221 (2008) 47–69.
[4] S. Daer, J. Kharraz, A. Giwa, S.W. Hasan, Recent applications of nanomaterials in water desalination: a critical review and future opportunities, Desalination, 367 (2015) 37–48.
[5] T. Humplik, J. Lee, S.C.O'Hern, B.A. Fellman, M.A. Baig, S.F. Hassan, M.A. Atieh, F. Rahman, T. Laoui, R. Karnik, E.N. Wang, Nanostructured materials for water desalination, Nanotechnology, 22 (2011) 292001–1–20.
[6] F. Perreault, A.F. de Faria, M. Elimelech, Environmental applications of graphene-based nanomaterials, Chem. Soc. Rev., 44 (2015) 5861–5896.
[7] D. Chohen-Tanugi, J.C. Grossman, Mechanical strength of nanoporous graphene as a desalination membrane, Nano Lett., 14 (2014) 6171–6178.

[8] L.F. Greenlee, D.F. Lawler, B.D. Freeman, B. Marrot, P. Moulin, Reverse osmosis desalination: water sources, technology, and today's challenges, Water Res., 43 (2009) 2317–2348.
[9] S. Porada, R. Zhao, A. Van der Wal, V. Presser, P. Biesheuvel, Review on the science and technology of water desalination by capacitive deionization, Prog. Mater Sci., 58 (2013) 1388–1442.
[10] M.E. Suss, S. Porada, X. Sun, P.M. Biesheuvel, J. Yoon, V. Presser, Water desalination via capacitive deionization: what is it and what can we expect from it?, Energy Environ. Sci., 8 (2015) 2296–2319.
[11] X. Gao, S. Porada, A. Omosebi, K.-L. Liu, P.M. Biesheuvel, J. Landon, Complementary surface charge for enhanced capacitive deionization, Water Res., 92 (2016) 275–282.
[12] M. Qin, A. Deshmukh, R. Epztein, S.K. Patel, O.M. Owoseni, W.S. Walker, M. Elimelech, Comparison of energy consumption in desalination by capacitive deionization and reverse osmosis, Desalination, 455 (2019) 100–114.
[13] M.A. Anderson, A.L. Cudero, J. Palma, Capacitive deionization as an electrochemical means of saving energy and delivering clean water. Comparison to present desalination practices: will it compete?, Electrochim. Acta, 55 (2010) 3845–3856.
[14] B. Jia, L. Zou, Wettability and its influence on graphene nansoheets as electrode material for capacitive deionization, Chem. Phys. Lett., 548 (2012) 23–28.
[15] S. Yamaguchi, Nanoionics-Present and future prospects, Sci. Technol. Adv. Mater., 8 (2007) 503–503.
[16] A.G. El-Deen, R.M. Boom, H.Y. Kim, H. Duan, M.B. Chan-Park, J.-H. Choi, Flexible 3D nanoporous graphene for desalination and bio-decontamination of brackish water via asymmetric capacitive deionization, ACS Appl. Mater. Interfaces, 8 (2016) 25313–25325.
[17] V. Chabot, D. Higgins, A. Yu, X. Xiao, Z. Chen, J. Zhang, A review of graphene and graphene oxide sponge: material synthesis and applications to energy and the environment, Energy Environ. Sci., 7 (2014) 1564–1596.
[18] C. Tsouris, R. Mayes, J. Kiggans, K. Sharma, S. Yiacoumi, D. DePaoli, S. Dai, Mesoporous carbon for capacitive deionization of saline water, Environ. Sci. Technol., 45 (2011) 10243–10249.
[19] S. Porada, L. Weinstein, R. Dash, A. Van der Wal, M. Bryjak, Y. Gogotsi, P.M. Biesheuvel, Water desalination using capacitive deionization with microporous carbon electrodes, ACS Appl. Mater. Interfaces, 4 (2012) 1194–1199.
[20] X. Xu, Z. Sun, D.H.C. Chua, L. Pan, Novel nitrogen doped graphene sponge with ultrahigh capacitive deionization performance, Sci. Rep., 5 (2015) 11225.
[21] P. Xu, J. Yang, K. Wang, Z. Zhou, P. Shen, Porous graphene: properties, preparation and potential applications, Chin. Sci. Bull., 57 (2012) 2948–2955.
[22] S.P. Koenig, L. Wang, J. Pellegrino, J.S. Bunch, Selective molecular sieving through porous graphene, Nat. Nanotechnol., 7 (2012) 728–732.
[23] S. Gupta, R. Meek, B. Evans, N. Dimakis, Graphene-based "hybrid" aerogels with carbon nanotubes: Mesoporous network–functionality promoted defect density and electrochemical activity correlations, J. Appl. Phys., 124 (2018) 124304–1–15.
[24] Water quality Determination of electrical conductivity, International standard ISO 7888 ; EPA method number 310.1, 1985.
[25] J. Xu, Y. Lin, J.W. Connell, L. Dai, Nitrogen-doped holey graphene as an anode for lithium-ion batteries with high volumetric energy density and long cycle life, Small., 11 (2015) 6179–6185.
[26] S. Gupta, A. Saxena, Nanocarbon materials: probing the curvature and topology effects using phonon spectra, J. Raman Spectrosc., 40 (2009) 1127–1137.
[27] M.S. Dresselhaus, A. Jorio, R. Saito, Characterizing Graphene, Graphite, and carbon nanotubes by Raman spectroscopy, Annu. Rev. Condens. Matter Phys., 1 (2010) 89–108.
[28] S. Gupta, E. Heintzman, J. Jasinski, Multiphonon Raman spectroscopy properties and Raman mapping of 2D van der Waals solids: graphene and beyond, J. Raman Spectrosc., 46 (2015) 217–230.
[29] F. Tunistra, J.L. Koenig, Raman spectrum of graphite, J. Chem. Phys., 53 (1970) 1126–1130.
[30] A. Jorio, M.M. Lucchese, F. Stavale, E.H.M. Ferreira, M.V.O. Moutinho, R.B. Capaz, C.A. Achete, Raman study of ion-induced defects in N-layer graphene, J. Phys.: Condens. Matter, 22 (2010) 334204–1–5.
[31] L.G. Conçado, A. Jorio, E.H.M. Ferreira, F. Stavale, C.A. Achete, R.B. Capaz, M.V.O. Moutinho, A. Lombardo, T.S. Kulmala, A.C. Ferrari, Quantifying defects in graphene via Raman spectroscopy at different excitation energies, Nano Lett., 11 (2011) 3190–3196.
[32] A. Das, S. Pisana, B. Chakraborty, S. Piscanec, S.K. Saha, U.V. Waghmare, K. Novoselov, H.R. Krishnamurthy, A.K. Geim, A.C. Ferrari, A.K. Sood, Monitoring dopants by Raman scattering in an electrochemically top-gated graphene transistor, Nat. Nanotechnol., 3 (2008) 210–215.
[33] E. Conway, Electrochemical Supercapacitors: Scientific Fundamentals and Technological Applications; Kluwer Academic/Plenum, New York, USA, 1999.
[34] S. Gupta, T. Smith, A. Banaszak, J. Boeckl, Graphene quantum dots electrochemistry and sensitive electrocatalytic glucose sensor development, Nanomaterials, 7 (2017) 301–1–20.
[35] A.S. Yasin, M. Obaid, I.M.A. Mohamed, A. Yousef, N.A.M. Barakat, ZrO_2 nanofibers/activated carbon composite as a novel and effective electrode material for the enhancement of capacitive deionization performance, RSC Adv., 7 (2017) 4616–4626.
[36] H. Li, L. Zou, L. Pan, Z. Sun, Novel graphene-like electrodes for capacitive deionization, Environ. Sci. technol., 44 (2010) 8692–8697.
[37] N.L. Ritzert, J. Rodriguez-Lopex, C. Tan, H.D. Abruňa, Kinetics of interfacial electron transfer at single-layer graphene electrodes in aqueous and non-aqueous solutions, Langmuir, 29 (2013) 1683–1694.
[38] L. Heller, J. Kong, K.A. Williams, C. Dekker, S.G. Lemay, Electrochemistry at single-walled carbon nanotubes: the role of band structure and quantum capacitance, J. Am. Chem. Soc., 128 (2006) 7353–7359.
[39] S. Gupta, N. Dimakis, Computational predictions of electronic properties of graphene with defects, adsorbed transition metal-oxides and water using density functional theory, Appl. Surf. Sci., 465 (2019) 760–772.